Article:
Rahaman, W, Smik, L, Köseoğlu, D et al. (6 more authors) (2020) Reduced Arctic sea ice extent during the mid-Pliocene Warm Period concurrent with increased Atlantic-climate regime. Earth and Planetary Science Letters, 550. 116535. ISSN 0012-821X

https://doi.org/10.1016/j.epsl.2020.116535

Reduced Arctic sea ice extent during the mid-Pliocene Warm Period concurrent with increased Atlantic-climate regime

*Waliur Rahaman[1], Lukas Smik[2], Deniz Köseoğlu[5], Lathika N[1], Mohd Tarique[1], Meloth Thamban[1], Alan Haywood[3], Simon T. Belt[2], J. Knies[4,5]

[1]National Centre for Polar and Ocean Research (NCPOR), Ministry of Earth Sciences, Vasco-da-Gama, Goa 403804, India

[2]School of Geography, Earth and Environmental Sciences, University of Plymouth, PL4 8AA, UK

[3]School of Earth and Environment, University of Leeds, Woodhouse Lane, Leeds, LS2 9JT, UK

[4]Geological Survey of Norway, N-7491 Trondheim, Norway

[5] CAGE – Centre for Arctic Gas Hydrate, Environment and Climate, Department of Geosciences, UiT The Arctic University of Norway, 9037 Tromsø, Norway

Revised submission to Earth and Planetary Science Letter (EPSL)

*Corresponding author (waliur@ncpor.res.in)

Orchid ID: https://orcid.org/0000-0001-6439-4529

Abstract

Quantifying the contribution of poleward oceanic heat transport to the Arctic Ocean is important for making future sea ice and climate predictions. To highlight its potential importance in a warmer world, we present a new record of water-mass exchange between the Atlantic and the Arctic Oceans using the authigenic neodymium isotopic composition of marine sediments from the Fram Strait during the past ~3.4 to 2.6 Ma. In this study, we target the mid-Pliocene Warm Period (mPWP: 3.264–3.025 Ma) of the Pliocene epoch, the most recent geological analogue for future climate change. We complement our semi-quantitative water mass exchange reconstruction with estimates of spring sea ice concentration based on source-specific biomarkers. Our estimates of volume transport of warm waters into the Arctic Ocean suggest long-term secular changes from the lowest during the Marine Isotope Stage M2 "glacial" (3.312–3.264 Ma), to near complete "Atlantification" of the Eurasian sector of the Arctic Ocean during the mPWP. Orbital forcing is found to be the dominant controlling factor for modulating northward volume transport of Atlantic-derived water masses, with consequential reduction in Arctic spring sea ice concentration by ~30-35%. Current generation models often produce diverging results, however, and have not yet been validated against proxy data in northern high latitude settings during the mPWP. Our new results of northward volume transport and sea ice extent therefore provide much needed input for validation of current generation models aimed at improving the robustness of future climate modelling in the Arctic.

Keywords: mid-Pliocene, North Atlantic Current, Arctic, Sea ice, Atlantification

1. Introduction

48 The most dramatic changes observed in the Arctic Ocean during the recent past are the
49 unprecedented reductions in sea ice extent and thickness (Kinnard et al., 2011). Although
50 coupled ice-ocean model simulations suggest that the recent warming in the Northern
51 Hemisphere is responsible for this decline (Petrie et al., 2015), there is disagreement
52 between data and models over the impact of atmospheric warming versus oceanic heat
53 transport on sea ice decline (Ding et al., 2018; Dowsett et al., 2012; Haywood et al., 2013).
54 Studies based on proxy reconstructions of heat and volume transport through the Fram
55 Strait (Spielhagen et al., 2011), and in-situ observations in the eastern Arctic Ocean
56 (Polyakov et al., 2017), suggest that enhanced oceanic heat transport by the North
57 Atlantic Current (NAC) over the past few decades likely explains the weakened
58 stratification, increased vertical mixing and reduced sea ice in the Atlantic sector of the
59 Arctic, collectively termed “Atlantification” (Polyakov et al., 2017; Spielhagen et al., 2011).
60 In order to improve our understanding about Arctic sea ice variability, particularly within
61 the current context of rapid global warming, it is imperative to reconstruct sea ice
62 conditions during previous warm climate states, and decipher the underlying mechanisms
63 that control its distribution. One such period in Earth’s history is the Pliocene (5.33–2.58
64 Ma), which experienced higher global temperatures than pre-industrial (Dowsett et al.,
65 2009), and was characterized by a gradual transition from relatively warm climates during
66 the Early Pliocene towards cooler conditions in the Late Pliocene. Some previous organic
67 geochemical-based proxy climate reconstructions for the Pliocene have been conducted
68 for the North Atlantic and Fram Strait (Clotten et al., 2018; Knies et al., 2002), and similar
69 studies have been carried out for other warm interglacials such as the Eemian (Marine

Isotope Stage (MIS) 5e) (Stein et al., 2017). However, the roles of atmospheric warming versus northward heat transport were not assessed as part of these studies.

Here we aimed to identify the potential impact of future changes in oceanic heat transport into the Arctic Ocean and the effects of "Atlantification" in a warmer than modern climate. To achieve this, we conducted a semi-quantitative assessment of northward volume transport of Atlantic water through the Fram Strait during a geological period when (1) climatic conditions in terms of temperature and atmospheric CO_2 level were analogous to modern/or future projected scenarios and (2) global oceanographic and tectonic settings were nearly identical to today. The mid-Pliocene Warm Period (mPWP: 3.264–3.025 Ma) is known to be warmer (globally) than today (Dowsett et al., 1992; Haywood et al., 2016), with atmospheric CO_2 concentrations estimated to be in the range 350-450 ppmv (Berends et al., 2019; Foster et al., 2017). Hence, the mPWP has been proposed as a possible reference for future warm climate states (IPCC, 2013). Confirmation of increased polar ocean heat transport and reduced sea ice in the Arctic Ocean during the mPWP (Raymo et al., 1996) would therefore be of clear benefit for the assessment of coupled ocean-ice-atmosphere model simulations of the mPWP (Haywood et al., 2016).

To achieve this objective, we first reconstructed an orbital-resolution record of watermass mixing between the NAC and Arctic-derived polar waters (PW) in the Fram Strait (Fig. 1), based on authigenic neodymium (Nd) isotopes (ε_{Nd}). The radiogenic isotope composition of Nd in seawater reveals changes in watermass mixing and circulation patterns due to its quasi-conservative behavior (Martin, 2002) and lower average oceanic residence time (360–2000 years) compared to the global ocean mixing time ~1500 years (Tachikawa et al., 1999) . Critically, in contrast to stable oxygen ($\delta^{18}O$)

or carbon isotope ($\delta^{13}C$) measurements, the Nd isotope ratios are not affected by isotopic fractionation resulting from any biological or other low-temperature processes, so represent a robust proxy for paleo-water mass circulation (Martin, 2002). In a modern context, the majority of Atlantic-derived water masses are transported northward into the Arctic Ocean along the Svalbard continental margin, which is the northernmost extension of the NAC (Fig. 1). This warm water submerges into the Arctic Ocean or is deflected westward and submerged southward below cold and less saline waters of the East Greenland Current (EGC). All of these modern water masses possess characteristic Nd isotope signatures (Fig. 1) (Laukert et al., 2017; Werner et al., 2014). Less radiogenic values are indicative of a stronger influence of NAC flowing into the Nordic Seas (present-day ε_{Nd} = -13.2 to -13.0) (Teschner et al., 2016) while more radiogenic Nd isotope signatures reflect enhanced contribution from Arctic-derived polar waters (PW) (Laukert et al., 2017) (e.g. ε_{Nd} = -9.9). For this study, an orbital-resolution (~5 ka) authigenic ε_{Nd} record was obtained through analysis of bulk sediments from Ocean Drilling Program (ODP) Hole 910C (hereafter referred to 910C) on the Yermak Plateau, eastern Fram Strait, (80°15.894'N, 6°35.430'E, water depth: 556.4 m) covering the interval between 3.4 Ma and 2.6 Ma. This new record is supplemented by a previously published low-resolution (60-70 ka) record of authigenic ε_{Nd} from ODP Hole 911A (80° 28.466′ N, 8° 13.640′ E, water depth: 902 m) (hereafter referred to 911A) at the eastern flank of the Yermak Plateau (Teschner et al., 2016).

To identify the corresponding changes in sea ice coverage and carbonate chemistry, the sea ice biomarker proxy IP_{25}, a related open-water highly branched isoprenoid (HBI) lipid (HBI III), and calcium carbonate ($CaCO_3$) abundance related to

carbonate chemistry and productivity/or preservation, were also analyzed. Over the last decade, source-specific highly branched isoprenoid (HBI) lipid biomarkers have emerged as reliable proxies for reconstructing past sea ice extent in the polar oceans (Belt, 2018 and references therein). The most frequently studied biomarker is the mono-unsaturated HBI IP_{25}, first identified in Arctic sea ice and sediments by Belt et al. (2007), and has since been used as a binary measure of seasonal Arctic sea ice in the past for time scales ranging from recent decades to several millions of years. Further, by combining sedimentary IP_{25} concentrations with those of various phytoplankton biomarkers in the form of the IP_{25}-phytoplankton (PIP_{25}) index, semi-quantitative estimates of sea ice extent can be achieved (Muller et al., 2011; Belt, 2018 for a review). Finally, when a further tri-unsaturated HBI (often referred to as HBI III; Belt et al., 2015) is used as the open water counterpart to IP_{25}, the resulting PIP_{25} index (i.e. $P_{III}IP_{25}$) exhibits a reasonably good linear relationship to spring sea ice concentration (%SpSIC) for the Barents Sea and neighboring regions (Smik et al., 2016).

North Atlantic and Arctic waters are characterized by distinct carbonate (e.g. alkalinity and pH) characteristics, so carbonate abundance in sediments from the Fram Strait (mixing zone) can be used to infer changes in carbonate productivity, preservation and dissolution resulting from variable paleo-oceanographic changes. For example, warm and carbonate-rich North Atlantic waters lead to better preservation compared to cold carbonate depleted Arctic waters. In some previous studies, therefore, high carbonate preservation in sediments from the Fram Strait has been attributed to increased influence of Atlantic water masses (e.g. Zamelczyk et al., 2014). In the Norwegian–Greenland Sea, high carbonate content has also been interpreted to reflect the influence of warm Atlantic

water masses, while low carbonate content were attributed to cold surface waters and increasing dilution by terrigenous material (Huber et al., 2000). Therefore, a combined authigenic Nd isotope and carbonate record from the Fram-Strait were employed in the present study to reconstruct northward volume and heat transport by the NAC.

2. Material and methods

Sediments of ODP Hole 910C (80°15.894' N, 6°35.430' E; water depth: 556.4 m) have been analyzed in this study. The deep-water Nd isotope signal was extracted from the Fe-Mn oxyhydroxide fraction of bulk sediment following the leaching procedure described below. Further details of Nd isotopes, highly branched isoprenoid biomarkers and calcium carbonate abundance measurements are given in the following sections.

2.1 Neodymium isotope analysis in authigenic fractions

We measured the neodymium (Nd) isotope composition in authigenic phases extracted from the bulk sediments of 910C. This new record of authigenic ε_{Nd} is supplemented by an earlier published low-resolution (60-70 ka) record from ODP Hole 911A at the eastern flank of the Yermak Plateau (Teschner et al., 2016). Therefore, for comparison, and to avoid discrepancies related to the analytical methods for the extraction of authigenic Nd from sediments and its isotope measurements, we adopted the same method of Teschner et al. (2016). The procedure thus began with extracting the past seawater signal contained in the diagenetic coatings from ~2 g of sample material with a 0.05 M hydroxylamine hydrochloride and 15% acetic acid solution (HH leach), buffered to a pH of ~3.5 to 4.0, without rinsing before the HH leach. The rare earth elements (REEs) in the solution were separated using cation exchange columns filled with AG50WX8 resin (mesh

200–400). Nd was separated from the other REEs using columns filled with Ln-Spec resin (50–100 mesh). Nd isotopes were analyzed using a multi-collector inductively coupled plasma mass spectrometer (MC-ICP-MS, Thermo Scientific Neptune Plus) at the National Centre for Polar & Ocean Research (NCPOR), Goa, India. All Nd isotope ratios ($^{143}Nd/^{144}Nd$) presented here were corrected for mass bias following an exponential law using the known value of $^{146}Nd/^{144}Nd$ of 0.7219. The instrument bias was normalized to the accepted $^{143}Nd/^{144}Nd$ value of the JNdi-1 standard of 0.512115 (Tanaka et al., 2000). Repeat measurements of the JNdi-1 standard yielded a long-term average reproducibility of ±0.3 ε_{Nd} (2σ; n = 103) over a period of nine months. Average procedural blank ascertained for Nd (n = 4) was 170 pg which is less than 1% of the total Nd analyzed in samples, so blank correction was not applied. All Nd isotope ratios are reported in epsilon notation according to Equation 1.

$$\varepsilon_{Nd} = \left[\frac{^{143}Nd/^{144}Nd_{sample}}{^{143}Nd/^{144}Nd_{CHUR}} - 1\right] \times 10^4 \qquad Eq\ (1)$$

In order to check the quality of the authigenic Nd isotope analyses, which includes chemical extractions of the authigenic Nd and its isotopic measurements, we analyzed a total of 16 replicates. Data from these replicates (with a variable range of ε_{Nd}) are highly consistent (Supplementary Fig. S1); majority are falling on the equiline (1:1 line) within their uncertainty.

2.2 HBI biomarkers

The HBI biomarkers IP_{25} and HBI III were extracted from freeze-dried subsamples (~2–4 g) from 910C. Samples were saponified in a methanolic KOH solution (~5 mL H_2O: MeOH (1:9); 5% KOH) for 60 min (70 °C). Hexane (3×2 mL) was added to the saponified content, with supernatant solutions, containing non-saponifiable lipids (NSLs), transferred

185 with glass pipettes to clean vials and dried over a gentle stream of N_2 to remove traces
186 of H_2O/MeOH. NSLs were then re-suspended in hexane (0.5 mL) and fractionated using
187 column chromatography (SiO_2; 0.5 g). Non-polar lipids, including IP_{25} and HBI III, were
188 eluted with hexane (6 mL). Each non-polar fraction was further purified to remove
189 saturated components using silver-ion chromatography (Belt et al., 2015) with saturated
190 compounds eluted with hexane (2 mL) and unsaturated compounds, including HBIs,
191 collected in a subsequent acetone fraction (3 mL). Prior to extraction, samples were
192 spiked with an internal standard (9-octylheptadec-8-ene, 9-OHD, 10 μL; 10 μg mL^{-1}) to
193 permit quantification of HBIs. Analysis of fractions containing IP_{25} and HBI III was carried
194 out using gas chromatography–mass spectrometry (GC–MS) following the methods and
195 operating conditions described elsewhere (Belt et al., 2012). Mass spectrometric analysis
196 was carried out in total ion current (TIC) and selected ion monitoring (SIM) modes. The
197 identification of IP_{25} and other HBIs was based on their characteristic GC retention indices
198 (e.g. RI_{HP5MS} = 2081 and 2044 for IP_{25} and HBI III, respectively) and mass spectra (Belt,
199 2018). Quantification of all HBIs was achieved by comparison of mass spectral responses
200 of selected ions (e.g. IP_{25}, *m/z* 350; HBI III, *m/z* 346) in SIM mode with those of the internal
201 standard (9-OHD, *m/z* 350) and normalized according to their respective instrumental
202 response factors, derived from solutions of known biomarker concentration, and sediment
203 masses (Belt et al., 2012).

204 Concentrations of IP_{25} and HBI III were combined in the form of the $P_{III}IP_{25}$ index
205 (Eq. 4), with the latter then used to provide semi-quantitative estimates of spring sea ice
206 concentration (SpSIC (%), Eq. 5) according to a recent regional calibration (Smik et al.,

2016). A root mean-square error of 11% associated with SpSIC estimates, was also calculated using regional calibration data (Köseoğlu et al., 2018; Smik et al., 2016)

$$P_{iii}P_{25} = \frac{IP_{25}}{(IP_{25} + (0.63 * HBI\ III)} \qquad Eq\ (4)$$

$$SpSIC\ (\%) = \frac{(P_{III}IP_{25} - 0.0692)}{0.0107} \qquad Eq\ (5)$$

Finally, we used the non-parametric CP3O algorithm from the R package ECP (R Core Team, 2018) to carry out change-point analysis on SpSIC estimates to identify significant shifts in the time series profile (Supplementary Fig. S2). All biomarker and %SpSIC data are provided in Supplementary Data 2.

2.3 Analysis of carbon

Analyses of total carbon (TC) and organic carbon (C_{org}) were performed with a LECO SC-632 at the Geological Survey of Norway, Trondheim. For TC determination, subsamples of 300-400 mg were combusted at 1350°C and the release of CO_2 was measured. For C_{org} analysis, sub-samples of 400-450 mg were placed in carbon-free pervious ceramic combustion boats. These were placed on a heating plate at 50 °C (± 5°C) and treated with 10 vol.% hydrochloric acid (HCl) to remove inorganic carbon (carbonate) and subsequently rinsed with distilled water and dried in the drying oven prior to analysis. Carbonate content was calculated as $CaCO_3$ = (TC- C_{org}) x 8.33 on the assumption that calcite is the dominant form in the carbonate fraction (Vogt et al., 2001). Results are provided in weight percentage (wt. %) and the standard deviation of the TC and C_{org} measurements based on the repeated measurements of a standard was ± 0.026 wt% (1σ, n=8) and ± 0.028 wt. % (1σ, n=11), respectively.

2.4 Age control for sediments deposited at ODP Hole 910C

The age constraints for 910C is based on correlation of bio-stratigraphic and magneto-stratigraphic datums with Hole 911A together with additional benthic stable isotope data from 910C for the Pliocene (2.44 – 5.76 Ma). The age model based on the tie points and associated uncertainties have already been discussed in previous studies (Grøsfjeld et al., 2014; Knies et al., 2014b; Mattingsdal et al., 2014). Briefly, five tie points formed the basis of the age model for our target interval between ~3.4 and 2.6 Ma in 910C (see Supplementary Table S1). Two tie-points at 190 mbsf and 305 mbsf inferred from seismic correlation between 910C and 911A mark the magneto-stratigraphic boundaries at 2.58 Ma (Matuyama/Gauss) and 3.6 Ma (Gauss/Gilbert) (Mattingsdal et al., 2014). Support for this age model is provided by the biostratigraphic "Datum A" (~2.78 Ma) at ~223 mbsf in 910C (Sato and Kameo, 1996) and the glacial-to-interglacial oscillations of the benthic $\delta^{18}O$ record of 910C (Knies et al., 2014a). Between "Datum A" (2.78 Ma) and the inferred Gauss/Gilbert boundary (3.6 Ma), we have originally applied an age model based on linear sedimentation rates between these two fix-points (Knies et al., 2014a). One major climate transition (i.e. MIS M2 glaciation) expressed by a sharp increase in the global $\delta^{18}O$ stack (Lisiecki and Raymo, 2005) (Supplementary Fig. S4) falls within our targeted time interval of 3.4 to 2.6 Ma. We used the more radiogenic ε_{Nd} peak at 260.4 mbsf in 910C as an additional tie point to define the MIS M2 glaciation (Supplementary Table S1), corresponding to a pronounced IRD pulse in Hole 911A (Supplementary Fig. S6). The calculated sedimentation rates between fix points either side of this new tie point are within the same order of magnitude (8 to 15 cm/ka) thus justifying this additional age fix point. The age of the "Datum A" corresponding to the depth 223 mbsf was constrained based on the occurrence of calcareous nanofossils in 910C

and 911A (Sato and Kameo, 1996) and is slightly shifted from the original age of 2.78 Ma (Knies et al., 2014b) to 2.83 Ma in the revised age model (Supplementary Table S1). Together with the new tie points for biostratigraphic "Datum A" and shifted radiogenic ε_{Nd} peak to MIS M2, we used the linear sedimentation rates between all tie points to establish the age model for 910C between 3.4 - 2.6 Ma (Supplementary Table S1). Based on the revised chronology, the most negative excursion in the authigenic ε_{Nd} profile is now shifted from 2.981 to 3.081 Ma, while the most positive excursion defines the MIS M2 glaciation (Supplementary Fig. S4). Considering the uncertainty in our age model, it might be challenging to resolve all individual peaks and troughs corresponding to glacial-interglacial stages in our proxy records of authigenic ε_{Nd}, biomarkers and $CaCO_3$; however, the most prominent excursions in our proxy records during the mPWP can be resolved with confidence, which is the primary target interval of the present study. All information on previously published and new tie points are provided in Supplementary Table S1.

3. Results

3.1 Authigenic ε_{Nd} record from the Yermak Plateau.

The new ε_{Nd} record from the Yermak Plateau allows identification of the maximum limit of water mass exchange between the NAC and Arctic derived Polar waters (PW), particularly during the major climatic transitions of the Pliocene to the earliest Pleistocene (3.4–2.6 Ma). These include the MIS M2 glaciation (3.312–3.264 Ma), the mPWP (3.264–3.025 Ma) and the intensification of Northern Hemispheric glaciation (iNHG) at ~2.7 Ma ago. The authigenic ε_{Nd} record shows long-term secular changes from -9.2 during the MIS

M2 glacial period to -14.4 (5.2 ε_{Nd} unit) during the mPWP; the modern value of -11.7 reported (Lambelet et al., 2016) from the core site falling within this range. Thereafter, an increasing trend up to -7.8 at ~2.6 Ma is clearly discernable, with several prominent positive excursions associated with iNHG cold stages (Fig. 2c). Our ε_{Nd} record for 910C exhibits a larger range (6.6 ε_{Nd} unit) compared to that of 911A (3.4 ε_{Nd} unit) (Teschner et al., 2016) within the time period 2.5–3.5 Ma (Fig. 2c), most likely due to the higher temporal resolution.

3.2 Biomarker and $CaCO_3$ records.

The occurrence of seasonal sea ice throughout the record is confirmed by the near continuous presence of the biomarkers IP_{25} and HBI III (Fig. 2d). Although the concentration of HBI III is mainly lower than that of IP_{25}, it is the more abundant biomarker during the mPWP (ca. 3.150–2.970 Ma), consistent with more productive open-water conditions, as also shown by the carbonate record, which reaches its highest values during the MIS KM1-K2 (~3.150-3.050 Ma) (Fig. 2f). The $CaCO_3$ abundance measured in the bulk sediments ranges from 0.5 to 6%; however, a sharp three fold increase from the mean value ~2% to 6% is evident during the mPWP, which coincides with the prominent negative excursion in the ε_{Nd} record (Fig. 2f).

4. Discussion

The authigenic ferromanganese oxyhydroxide fraction extracted from the bulk sediments has been demonstrated to record the ε_{Nd} signal of bottom waters of the Yermak Plateau (Teschner et al., 2016; Werner et al., 2014). Hence, temporal variations in authigenic ε_{Nd} during glacial-interglacial periods have been primarily attributed to watermass exchange

between the NAC and PW, changes in sediment provenance, and variable weathering input due to glacial erosion (Teschner et al., 2016). However, other factors/mechanisms that contributed to the past authigenic ε_{Nd} variability are discussed in the following section.

4.1 Factors contributing to past authigenic ε_{Nd} variability

ODP Hole 910C is placed in the mixing zone between Atlantic- and Arctic-derived waters (Fig. 1) and is therefore well suited to monitor the relative influence of two water masses: (i) relatively warmer, high salinity water (i.e. the NAC characterized by a less radiogenic Nd isotope signature and (ii) relatively cold and less saline water (i.e. Arctic-derived PW) characterized by more radiogenic Nd isotopes. In the open ocean away from ocean margins and regions of deep-water formation, Nd appears to behave quasi-conservatively (Rempfer et al., 2011). Therefore, the variability in authigenic ε_{Nd} record from the open ocean is mainly explained by the mixing of water masses with distinct ε_{Nd} signatures (Lang et al., 2016). However, contributions from other sources of dissolved Nd can substantially influence the authigenic ε_{Nd} record. Assuming that the modern geological and tectonic setting of the study region have largely remained stable over the past ~4.6 Ma (Knies et al., 2014a), we discuss the following potential mechanisms and factors that may have contributed to the variability and changes in the authigenic ε_{Nd} record of 910C: (i) changes in weathering regimes and sediment sources; (ii) boundary exchange processes; and (iii) volumetric exchange of the NAC and PW.

Dissolved radiogenic isotope signatures in seawater originate from weathering processes of the continental crust (Frank, 2002) and, therefore, the glacial-interglacial changes in chemical weathering could influence the ε_{Nd} record. Teschner et al. (2016) reconstructed past water mass mixing and erosional inputs prior and post intensification

of Northern Hemisphere glaciation (iNHG, ~2.7 million years ago) based on records of radiogenic isotopes of Sr, Nd and Pb at ODP Hole 911A. Changes in the authigenic ε_{Nd} record were highlighted for two different scenarios; (i) prior to the iNHG, the Pb and Nd isotopes composition was characterized by unradiogenic values and low variability due to the limited extent of ice sheets. These observations are consistent with earlier inferences from the Arctic Ocean (Haley et al., 2007) and suggest constant erosional supply of material to the Yermak Plateau, most likely from local sources (i.e. Svalbard). (ii) After the iNHG, conditions changed dramatically with higher-amplitude ε_{Nd} variability in both deep waters and detrital sediments inputs due to changes in weathering inputs associated with the waxing and waning of the Eurasian ice sheets, water mass exchange and increased supply of ice-rafted debris (IRD). Comparison of the IRD record (Knies et al., 2014b) with our ε_{Nd} record, shows higher IRD flux during the periods of M2 and iNHG (~2.7 Ma), and low and stable IRD fluxes during the mPWP (Supplementary Fig. S6). The latter corresponds to the IRD record from Site U1307 on Eirik Drift where coarse IRD is largely absent during the mPWP, and IRD is only present in small abundances during (de)glacials between ~3 Ma and 2.75 Ma. Therefore, higher variability in IRD supply and change of its sources could influence the authigenic ε_{Nd} record in 910C; however, this can be excluded for the interglacial periods prior to the iNHG, particularly during the mPWP. It is also important to note that the timing of the iNHGs was further shifted to post MIS G2 (2.64 Ma) based on the Pb isotope and geochemical studies of the IRD on the lower eastern flank of the Reykjanes Ridge (Bailey et al., 2013). Therefore, we suggest that the observed variability and changes in the radiogenic Nd isotope record in 910C is affected by glacial weathering input probably during the MIS M2 glaciation and after the iNHG. In

contrast, it is unlikely to be significantly affected by the changes in chemical weathering inputs and/sediment transport from distant sources during our targeted time interval of mPWP due to the stability of the climatic conditions and glacial erosion was rather limited.

The chemical weathering of Iceland-derived basaltic material can influence the Nd isotope composition of the NAC resulting in a shift towards more radiogenic values. However, in an earlier study, it has been suggested that present day exchange with Iceland derived basaltic material does not affect the deep water ε_{Nd} signature of the main path of North Atlantic inflow, although it can influence the signature of southward flowing currents such as the East Greenland Current (Chen et al., 2012; Lacan and Jeandel, 2004).

Seawater interactions with the continental margins (boundary exchange) could be a potential source for radiogenic isotope signatures of seawater, particularly in the Nordic Seas where basaltic formations are highly susceptible to dissolution and exchange with seawater (Chen et al., 2012; Lacan and Jeandel, 2004). The effects of boundary exchange have been reported from different continental margins in the subpolar regions including the Nordic Seas, and model results confirmed the importance of this input mechanism (Rempfer et al., 2011). Due to the large shelf areas of the Arctic Ocean, boundary exchange might be expected to be significant, although the water column data available so far do not provide clear evidence for this process (Andersson et al., 2008). Further, Laupkert et al (2017) suggested recently that ε_{Nd} values around -10 are present in the eastern and western Fram Strait below ~500 m, implying that there is no evidence for boundary exchange processes influencing the ε_{Nd} record to a significant extent on the Yermak Plateau.

In summary, with the absence of any significant ice-rafting prior to ~2.7 Ma (except MIS M2) in the Nordic Seas (Fig. 2e), increased sea surface temperatures (SST) by 3–7°C (Lawrence et al., 2009) between 3.4 and 2.6 Ma compared to the Holocene mean annual SST (Fig. 2g; dashed line) (Calvo et al., 2002), and thus no widespread Northern Hemisphere glacial advances, we attribute the large range in ε_{Nd} (-14.8 to -9.0) in 910C prior to the iNHG to changes in watermass circulation rather than to variable glacial weathering input. As such, the prominent negative excursion in the ε_{Nd} record during the mPWP (i.e. -14.4 ε_{Nd} units; Fig. 2c) is most likely due to an increase in volume transport of the NAC, resulting in an Atlantic-dominated climate regime of the Eurasian sector of the Arctic Ocean. Further, the prominent negative excursion in ε_{Nd} record coincides with a sharp three-fold increase in $CaCO_3$ abundance during the mPWP (Fig. 2f). This suggests an increased flow of warm NAC with higher pH resulted in better preservation of carbonate and/or increase in productivity during interglacial periods in the eastern Fram Strait (Supplementary Figs. S7b, d, e), consistent with earlier reports from modern and Quaternary sediments (Huber et al., 2000).

To test the hypothesis of increased “Atlantification” and its concurrent sea ice decline further, we quantified the volumetric changes of the AW-derived water masses and sea ice concentration at 910C using (1) a simplified binary mixing model by constraining the end member values of ε_{Nd} for two water masses and (2) semi-quantitative estimates of spring sea ice concentration (%SpSIC) based on a regional calibration of biomarker distributions in modern sediments (Smik et al., 2016).

4.2 Quantifying water mass exchange based on authigenic ε_{Nd} record

Compilation and reassessment of seawater Nd data from the literature shows that the characteristic NAC ε_{Nd} signature near its origin in the inter-gyre region (north of 46° N) displays ε_{Nd} values between -14.0 ± 0.3 and -15.1 ± 0.3 (Dubois-Dauphin et al., 2017), which changes gradually during transport across the Arctic Mediterranean due to mixing of more radiogenic signatures of PW (ε_{Nd} = -9.9 ± 0.7, 1 SD (standard deviation) and [Nd] =27.1) (Laukert et al., 2017). We have assigned ε_{Nd} and [Nd] values for the NAC (-15 ± 1 (1 SD) and 16 ± 1 pmol/kg) and PW (-9.9 ± 1 (1 SD) and 27± 1pmol/kg) end-members, respectively, which are clearly distinct from the modern value in the Fram Strait (mean ε_{Nd} = -11.7 ± 0.8 (2SD)) (Laukert et al., 2017). With this identification of suitable end-member values for ε_{Nd}, we therefore adopt a simple binary mixing approach for the determination of the percentage Atlantic water component (%AWC) on the assumption that Nd behaves quasi-conservatively and end-member compositions were invariant during the studied time interval. Such assumptions are discussed in more detail in the Supplementary Note 2. Meanwhile, we note that this method was successfully employed in a previous study (Lang et al., 2016) using a Nd isotope record from the late Pliocene (3.3–2.4 Ma ago) to quantify the mixing proportion of southern source water and north Atlantic deep water (NADW) in the North Atlantic.

4.2.1 Binary estimates of Atlantic water mass mixing using authigenic ε_{Nd} record

We have used the ε_{Nd} record from 910C to generate the semi-quantitative estimate of water-mass mixing between NAC and PW during the Late Pliocene to early Pleistocene (~3.4 - 2.6 Ma). The underlying assumptions of this approach are: (i) Nd isotopes exhibit quasi-conservative behaviour, (ii) mixing of Atlantic- and Arctic-derived waters at 910C is binary, and (iii) modern day end-members have been invariant between 3.4 and 2.6 Ma.

We used the following binary mixing equation constrained by our current understanding of end-member compositions:

$$\varepsilon_{Nd_{910C}} = \frac{\varepsilon_{Nd_{AW}} * C_{AW} * f_{AW} + \varepsilon_{Nd_P} * C_{PW} * f_{PW}}{C_{AW} * f_{AW} + C_{PW} * f_{PW}} \qquad Eq\ (2)$$

$$f_{AW} + f_{PW} = 1 \qquad Eq\ (3)$$

where $\%AWC_{\varepsilon_{Nd}} = f_{AW} * 100$ is the relative contribution of Atlantic water component to 910C ($\%PWC_{\varepsilon_{Nd}}$ = 100 - $\%AWC_{\varepsilon_{Nd}}$), C_{PW} and C_{AW} represent the concentration of Nd in the Arctic (PW) and the Atlantic (AW), ε_{Nd910C} is the value of Nd isotope compositions of sediment leach from 910C, and ε_{AW} and ε_{PW} are the end-members of isotope composition of Atlantic and Arctic water masses, respectively. f_{AW} and f_{PW} represent the fractions of Nd coming from the Atlantic (AW) and Arctic (PW) waters.

In order to validate the use of this binary mixing model to 910C, we also calibrated our approach by comparison of semi-quantitative estimates of modern day volume transport with in situ observations. We thus estimated the modern day volume transport of NAC using a contemporary ε_{Nd} value at the borehole site of 910C and compared that with a mooring-based observation (Beszczynska-Moeller et al., 2012). Our estimate of %NAC based on ε_{Nd} (47 ± 9%) (Supplementary Fig. S9) compares well with a value of 45 ± 5% (Supplementary Fig. S9b) measured from an array of moorings in Fram Strait (78° 50′ N) over the period 1997–2010 (Beszczynska-Moeller et al., 2012).

We have determined the uncertainty associated fractions of NAC volume estimates using a Monte-Carlo error propagation method with 10,000 iterations in MATLAB, which is represented as an error envelop (at 95% confidence) (Fig. 3a).

433 However, we offer some caution that our %NAC estimates may be subject to changes in
434 the future when more suitable archives allow generation of orbital resolution records of
435 NAC and PW end-member behaviour. For now, the uncertainties reported here for our
436 ε_{Nd}-based estimates of %NAC may be underestimated due to limited knowledge of end-
437 member ε_{Nd} values for Atlantic and Arctic waters. On the other hand, our main conclusions
438 over our targeted time interval (3.4 – 2.6 Ma) are not influenced by such uncertainties.

439 Our estimates of %AWC in 910C indicate three distinct peaks with values close to
440 100%, indicating the presence of a dominant Atlantic watermass in the water column
441 during the three interglacial events (Haywood et al., 2013) (i.e. MIS KM3, K1, and G17)
442 within or close to the mPWP; albeit within the limitation of the age constraints of 910C
443 (Fig. 3 a). For MIS KM5c, with near-modern orbital configuration, the %AWC (51 ± 11%)
444 was similar to today (45 ± 5%) (Beszczynska-Moeller et al., 2012; Zhang et al., 2013) but
445 was close to ~0% during the preceding MIS M2 glaciation (3.305–3.285 Ma) (Fig. 3a),
446 consistent with previous observations of a weaker NAC and concurrent cooling in the
447 circum-Arctic (De Schepper et al., 2015). Importantly, although %AWC estimates for the
448 glacial periods (M2 and iNHGs) might potentially suffer higher uncertainty due to
449 enhanced IRD flux and weathering inputs associated with higher glacial activity, such
450 effects during the mPWP are likely insignificant, in practice, due to the relatively stable
451 climate and lower IRD fluxes (Blake-Mizen et al., 2019; Knies et al., 2014a) (Fig. 2e and
452 Supplementary Fig. S6). Pertinent to our reconstructed reduced flux of %AWC during the
453 M2 glaciation, we note that a similar situation has been reported for MIS6 based on
454 authigenic coupled isotope records of Nd and Hf from the central Arctic Ocean (Chen et
455 al., 2012).

456 **4.2 Sea ice reconstruction**

457 Extensive sea ice cover (>60% SpSIC) prevailed from 3.36–3.18 Ma, including maximum
458 extent during MIS M2 (Fig. 3b). Thereafter, %SpSIC reduced substantially. According to
459 Smik et al. (2016), biomarker-based %SpSIC estimates above ca. 68% also imply the
460 occurrence of some summer sea ice (>5% SuSIC) (Supplementary Fig. S3). Similarly,
461 while the occurrence of some summer sea ice was a common feature up to ca. 3.18 Ma
462 (Fig. 3b), coincident with consistently low %AWC (i.e. below the modern value of 45%;
463 Fig. 3a), ice-free summers were likely a common feature at the Yermak Plateau
464 thereafter, especially during the mPWP. Change-point analysis carried out on our
465 %SpSIC estimates shows a statistically significant decrease of ca. 30–35% starting at ca.
466 3.15 Ma before increasing again at ca. 2.97 Ma (Supplementary Fig. S2). Prior to this,
467 extensive sea ice cover similar to the modern (spring) maximum prevailed, including
468 maximum extent during MIS M2 when the %AWC was at a minimum (Fig. 3a, b). The
469 reduction in SpSIC during the mPWP likely reflects a response to increased %AWC,
470 analogous to observations made for eastern Fram Strait (Spielhagen et al., 2011) and the
471 Barents Sea spanning recent decades/centuries (Cabedo-Sanz and Belt, 2016). Similar
472 observations have been reported for the Early Holocene and the Last Interglacial (MIS
473 5e/Eemian), implying that increased Atlantic Water inflow is one important factor
474 controlling sea ice conditions in an area covering northern Svalbard/Yermak Plateau and
475 the northern Barents Sea continental margin (Müller et al., 2012; Belt et al., 2015; Stein
476 et al., 2017). According to our SpSIC estimates, maximum sea ice extent during the
477 mPWP exhibited a closer resemblance to that of modern-day late summer (i.e. minimum)
478 conditions (Fig. 3b). These new data support the boundary conditions used in the

Pliocene Research, Interpretation and Synoptic Mapping (PRISM) project, which assumes a conservative sea ice extent, an ice-free Arctic Ocean in summer, and winter sea ice conditions approximately equivalent to modern summer ice extent (Dowsett et al., 2010).

4.3 Forcing factors modulating North Atlantic volume transport and its impact

Our new reconstructions of watermass mixing and carbonate abundances follow the periodicities of eccentricity (~100 ka), obliquity (~40) and precessional cycles (~20 ka) (Figs. 4a, b). Further, the %AWC and %SpSIC records show good alignment with the eccentricity (Fig. 4c) and summer insolation in the northern hemisphere (Fig. 5b), implying orbitally-paced control over changes to oceanic heat flow into the Arctic Ocean. Cross wavelet analysis highlights the common highest power between these two time series in colour bands (Fig. 4c). The vector arrows indicate an in-phase relation (pointing rightward) during 3.2 – 2.9 Ma at the eccentricity band (64 – 128 ka), implying that orbitally-controlled, enhanced NAC resulted in an increase in marine productivity and reduction in sea ice coverage during the mPWP (Supplementary Fig. S7c, d). In particular, during the three interglacials with high eccentricity (i.e. KM3, K1, and G17; Fig. 5a, d), increased seasonality combined with warmer summers (higher solar insolation) in the Northern Hemisphere (Fig. 5a, b) may have resulted in an increased oceanic heat transport with consequential decline in Arctic sea ice extent and polar amplification of this warming. Alternatively, an orbitally-forced reduction in Arctic sea ice coverage may have changed buoyancy and salinity in the Atlantic, and thus been responsible for increased northward ocean heat transport during mPWP interglacials leading to a strongly positive ice-albedo feedback. Our proxy data do not reveal any correspondence with variable

atmospheric CO_2 estimates (Figure 5c, d and e) implying only a minor influence of greenhouse gas-derived radiative forcing in modulating NAC heat transport and reduction in Arctic sea ice. Further, tectonic changes could have driven circulation changes as has been reported for the Bering Strait and Nordic Sea related to reconfiguration of oceanic gateways (De Schepper et al., 2015; Horikawa et al., 2015). However, the strong signal of orbital cycles in our proxy records clearly indicate that the orbital forcing played the dominant role over all other controlling factors.

Based on multi-proxy records, it has been inferred that the Atlantic Meridional Overturning Circulation (AMOC) was significantly stronger in the mPWP compared to today (Raymo et al., 1996; Frank et al., 2002; Dowsett et al., 2009), which could have contributed to enhanced northward heat transport during the mPWP interglacials (Dowsett et al., 2009; Lawrence et al., 2010; Naafs et al., 2012), consistent with our findings. However, the exact mechanism(s) responsible for changes in northward heat transport remain a topic of debate (Haywood et al., 2016; Haywood et al., 2013; Zhang et al., 2013), but could potentially be resolved through further ocean modelling studies that integrate the new proxy data presented herein.

Regardless of the ultimate driver(s), our estimates of %AWC show a clear dominance of a warm and well-mixed Atlantic-dominated climate regime in the Eurasian Arctic during MIS KM3, K1, and (within the given age uncertainties) G17, with lower than modern sea ice extent (including ice-free summers) and higher marine productivity, consistent with modeled and reconstructed amplification of Arctic surface temperatures (Ballantyne et al., 2013), and a rise in annual mean surface air temperatures between 4°C to 5°C (Δt= Plio-KM5c – pre-industrial) (Prescott et al., 2018). This implies that the

increase in %AWC with concurrent reduction in %SpSIC during these mPWP interglacials resembles modern observations of an advanced “Atlantification” of the study region (Cabedo-Sanz and Belt, 2016; Naafs et al., 2010; Spielhagen et al., 2011).

The conclusion of increased “Atlantification” of the Arctic during the mPWP from our new proxy records from the Atlantic-Arctic gateway confirms previous studies from lower latitudes a (Naafs et al., 2010; Raymo et al., 1996). Since current generation models have not yet been validated against any proxy-based observations of “Atlantification” in the Eurasian sector of the Arctic during the mPWP, our new Nd isotope, biomarker and $CaCO_3$ records thus provide important input for testing the robustness of future climate modelling for northern high latitude settings.

5. Conclusions

Our new Nd isotope record of past water mass exchange in the Atlantic-Arctic gateway relative to the modern-day setting suggests a near doubling of NAC volume transport during mPWP interglacials KM3, K1, and G17 with different orbital configurations and thus stronger seasonality than today. This resulted in a warm and well-mixed Atlantic-dominated climate regime (“Atlantification”) of the Eurasian sector of the Arctic Ocean, reduced spring sea ice concentration, and the possibility of ice-free conditions during summers. In contrast, the mPWP interglacial with near-modern orbits (MIS KM5c) does not show significant deviation from today’s NAC volume transport or sea ice extent. This study demonstrates a dominant role of orbital forcing in modulating northward ocean heat transport and Arctic sea ice coverage during the mPWP. It also highlights the importance of improving data-model comparison studies for the Arctic Ocean that integrate reconstructions of water mass flow and ocean circulation, as well as

548 temperature and sea ice, for climate states of the past that may be analogous to the
549 future.

550 **Data availability**

551 All the data are provided in the supplementary and also will be archived in PANGEA upon acceptance of
552 the manuscript.

553 **Code availability**

554 The MATLAB codes for uncertainty estimates on the volumetric water fractions of Atlantic water are
555 available from the corresponding author W. Rahaman on request.

556 ## Acknowledgements

557 We acknowledge Ministry of Earth Sciences, Govt. of India, NCPOR, and Research Council of
558 Norway through its funding scheme for CAGE (223259) and PACT (248793). We thank Manish
559 Tiwari for his support as a Co-PI in the PACT project. We thank C Torrence, GP Compo, A
560 Grinsted, JC Moore, and S Jevrejeva for MATLAB codes. Authors thank Priya Lokhande for initial
561 handling of the sample for Nd isotope chemistry and Rohit Srivastava for providing MATLAB
562 codes for Monte-Carlo error propagation on the water fractions estimates. Finally, we thank two
563 anonymous reviewers who provided supportive and constructive feedback on the initial version
564 of this manuscript.

565 ## Author contributions

566 W.R., J.K. and M.T. designed the study. W.R., J.K., S.T.B and A.H wrote most of the text. Analysis
567 of model results was completed by A.H and J.T. Mo.T. and L.N. analyzed authigenic Nd isotope
568 compositions in bulk sediment. L.S, D.K and S.T.B. measured the concentrations of the IP_{25} and
569 HBI III biomarkers in bulk sediments and interpreted outcomes. All authors contributed to
570 interpreting results, discussion and improvement of this paper.

Competing interests

The authors declare no competing interests.

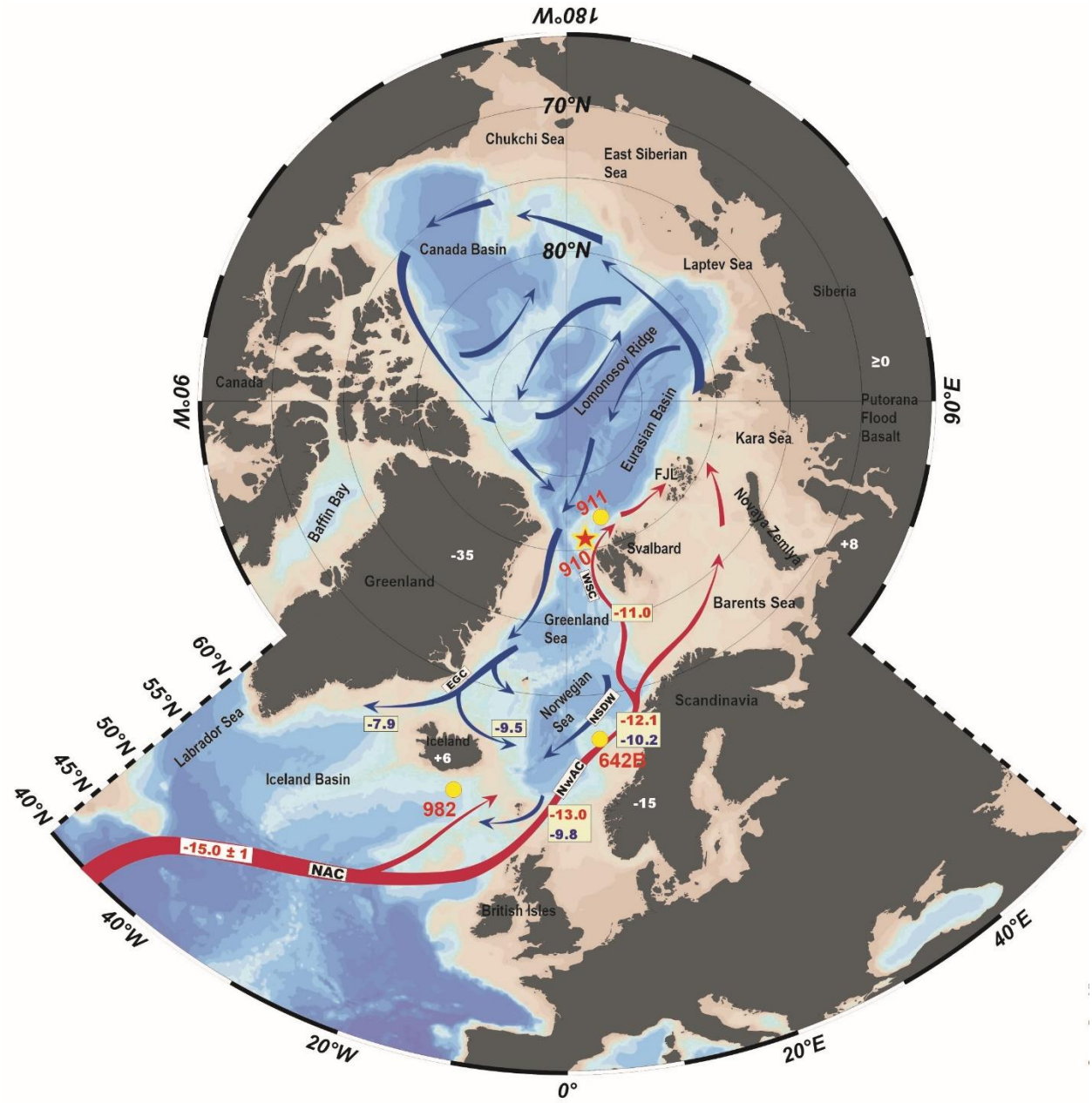

Fig. 1. Water mass circulation and their characteristic Nd isotope compositions. Locations of ODP Sites 910 (red star) and 911 (filled yellow circle) with schematic flow paths of the main water masses in the

577 northern North Atlantic and Nordic Seas and their present-day ε_{Nd} signatures(Teschner et al., 2016). Dark
578 red arrows mark the warm inflowing Atlantic water; dark blue arrows represent the cold deep and surface
579 water masses flowing out of the Arctic Ocean(Andersson et al., 2008; François and Catherine, 2004; Lacan
580 and Jeandel, 2004). White numbers mark the average ε_{Nd} values of the bedrocks of Svalbard(Tütken et al.,
581 2002), the Norwegian Caledonian Margin and Iceland(Laskar et al., 2004), the Putorana basalts in Russia
582 (Sharma et al., 1992), and Greenland (François and Catherine, 2004). Positions of ODP site 982 (58° N,
583 16° W) and ODP Hole 642B (67° 20′ N, 2° 90′ E) are shown.

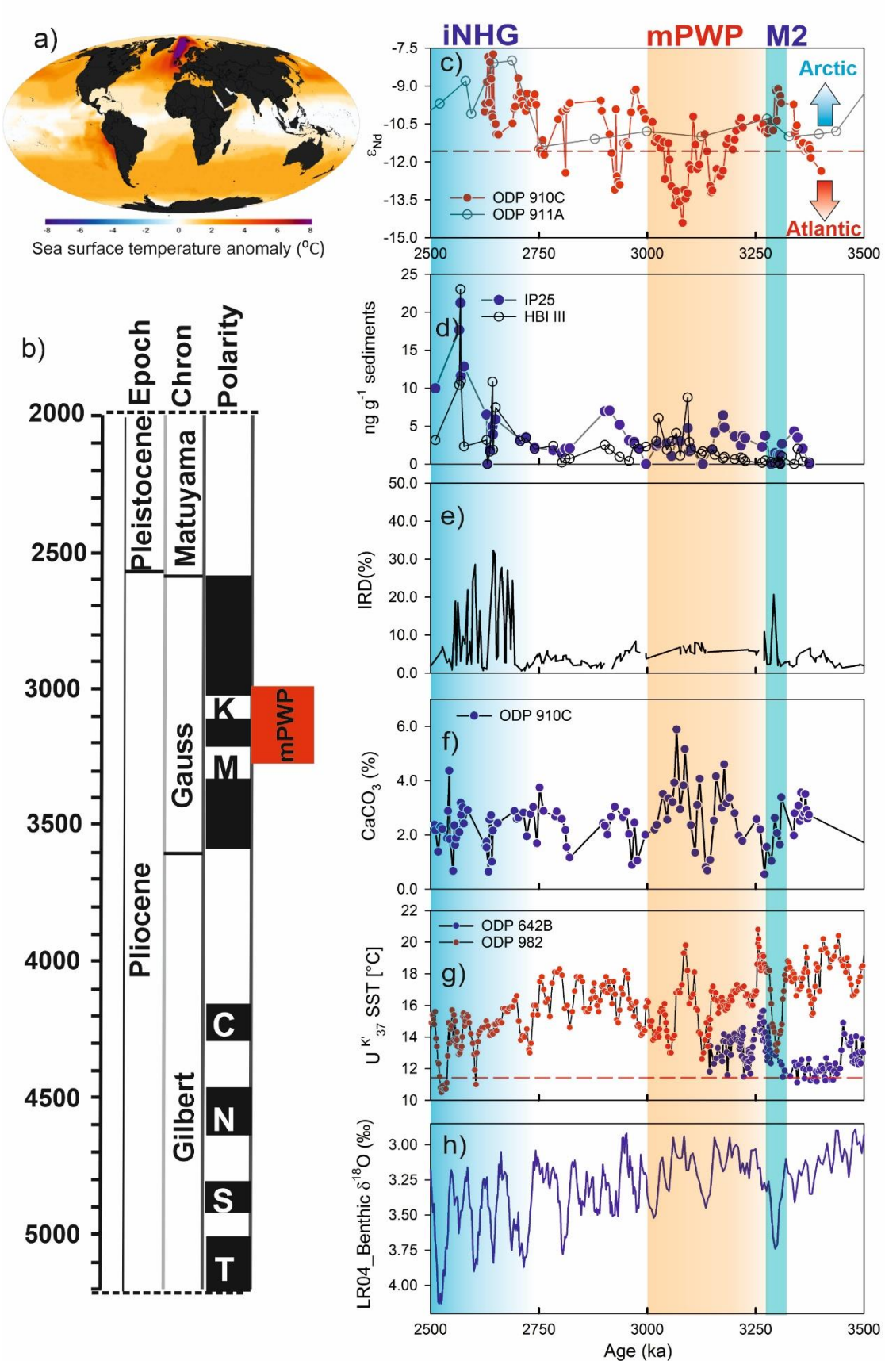
a)
Sea surface temperature anomaly (°C)
b)
Epoch
Chron
Polarity
Pleistocene
Matuyama
Gauss
Pliocene
Gilbert
mPWP
K
M
C
N
S
T
2000
2500
3000
3500
4000
4500
5000
iNHG
mPWP
M2
c)
Arctic
Atlantic
ODP 910C
ODP 911A
ε_{Nd}
d)
IP25
HBI III
ng g^{-1} sediments
e)
IRD(%)
f)
ODP 910C
$CaCO_3$ (%)
g)
ODP 642B
ODP 982
$U^{K'}_{37}$ SST [°C]
h)
LR04_Benthic $\delta^{18}O$ (‰)
Age (ka)

584

Fig. 2. Water mass exchange and associated changes in the Fram Strait during the Late-Pliocene and Pleistocene (a) Sea surface temperature (SST) anomalies during the mPWP (~3.3 – 3.0 Ma) compared to today (Dowsett et al., 2009). b) Pliocene-Pleistocene time scale with paleo-magnetic reversals. Red block represents the time slice of mPWP. c) Authigenic ε_{Nd} record from 910C (this study) and 911A (Teschner et al., 2016). d) Record of sea ice and open water biomarkers IP_{25} and HBI III. (e) Record of IRD (%) from ODP site 911A (Knies et al., 2014b). f) Record of $CaCO_3$ abundance (wt. %). g) Record of alkenon UK_{37} derived SST at ODP Sites 982(Lawrence et al., 2009) (58° N, 16° W) and ODP Hole 642B(Bachem et al., 2017) (67° 20′ N, 2° 90′ E). Dashed lines indicate Holocene average SSTs for the Norwegian Sea(Calvo et al., 2002) at 11.6 °C. h) Benthic $\delta^{18}O$ (LR04) stack(Lisiecki and Raymo, 2005). The shaded bands represent the major climatic transitions: M2 glaciation (blue shade, 3.312–3.264 Ma), mid-Pliocene Warm Period (mPWP) (brown shade, 3.3–3.0 Ma) and intensification Northern Hemisphere glaciation (iNHG, ~2.7 Ma).

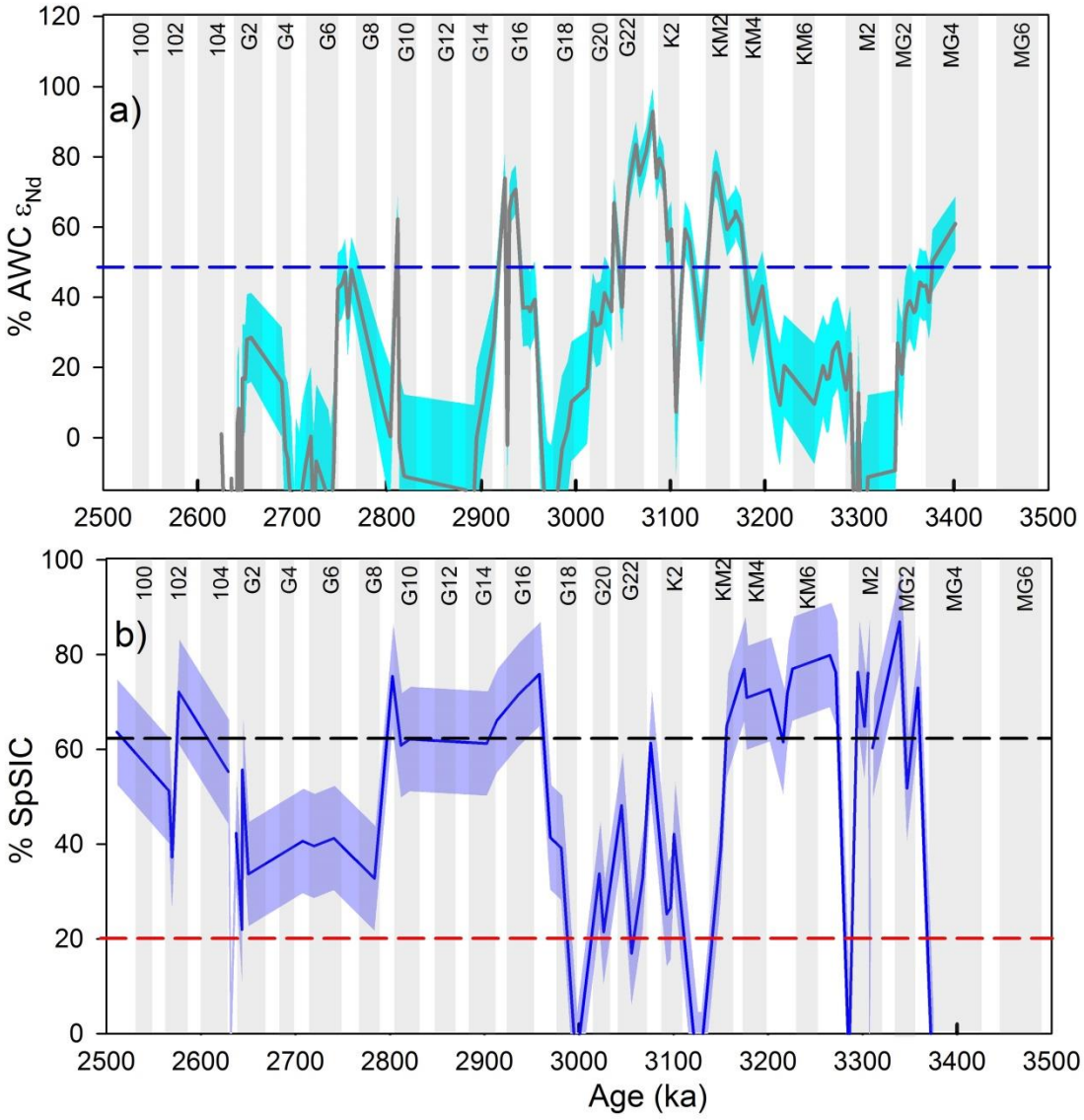

608

609 **Fig. 3. North Atlantic (NAC) volume transport and corresponding Arctic Sea Ice changes**. a) Fraction
610 of Atlantic Water Component (%AWC$_{\varepsilon Nd}$). Dark gray line: Best estimate. Shading: 95% confidence interval.
611 Blue dashed line indicates modern Atlantic flow based on mooring estimate (Beszczynska-Moeller et al.,
612 2012). (b) Spring sea ice (%). Solid blue line represents mean value. Blue shade represents root-mean-
613 square error (RMSE) on the mean value. Blue and red dashed horizontal lines represent the modern mean
614 (1988-2017, NSIDC) sea ice maximum (62%, Apr-June; spring) and minimum (20%, September; late
615 summer) concentrations at the core site.

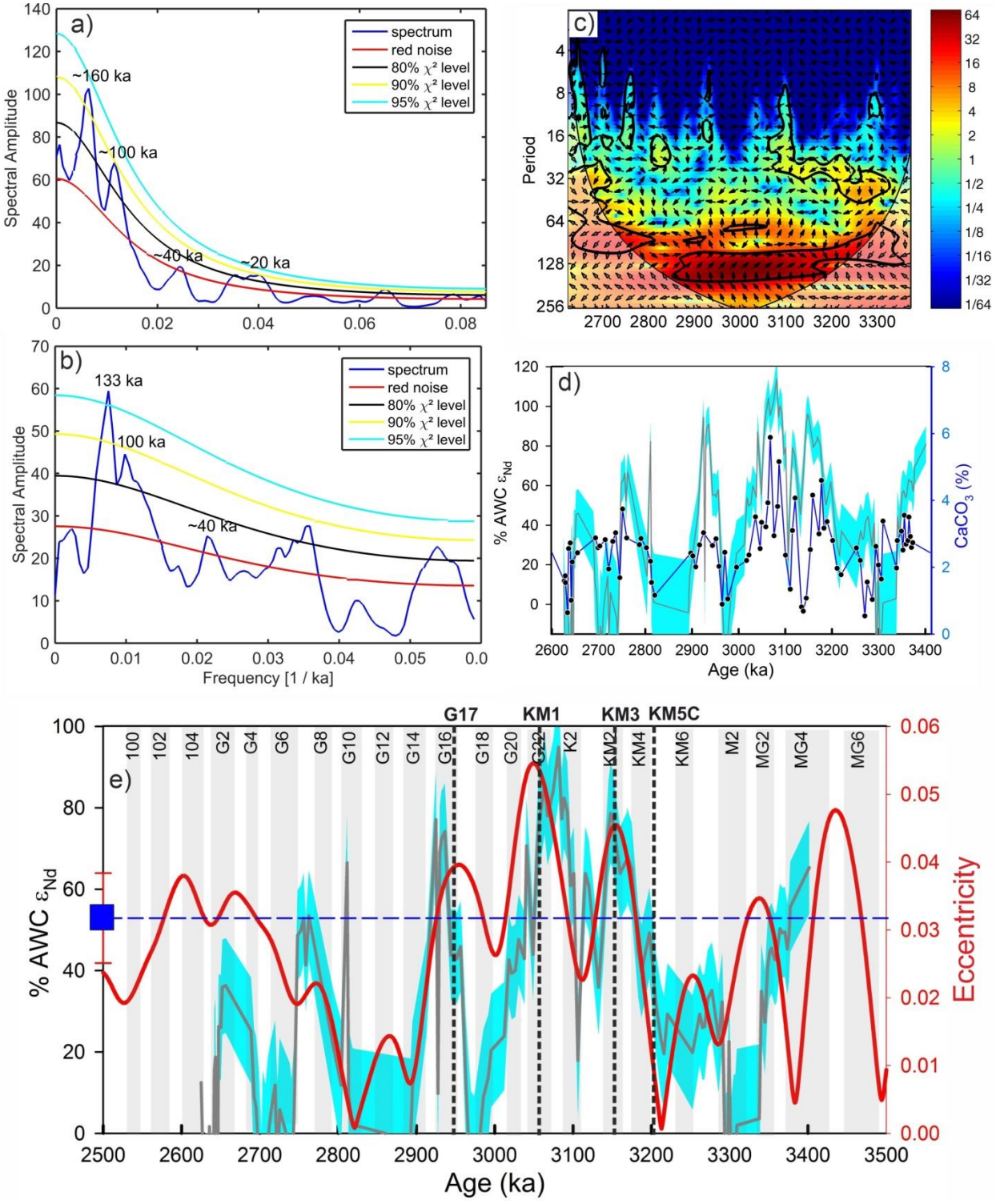

Fig. 4. Identification of orbital cycles in proxy records. Power spectrum analysis of (a) NAC volume transport and (b) $CaCO_3$ abundance (%) records from the Yermak Plateau. They show periodicities of orbital

cycles at different significance level. c) Cross wavelet analysis of two time series highlights the common highest power between these two time series which is highlighted in color code. Vector arrow indicates phase relation between the time series. The 5% significance level against red noise is shown as a thick contour. The thin solid line indicates cone of influence. The relative phase relationship is shown as arrows (with in-phase pointing right, anti-phase pointing left, and ε_{Nd} leading $CaCO_3$ by 90° pointing straight down and vice versa). d) Comparison of the record of NAC with $CaCO_3$ percentage, an indicator of marine productivity. Both the curves overall follow the same pattern; the highest abundance in calcium carbonate and thus the highest productivity was observed during mPWP when NAC flow was maximum.

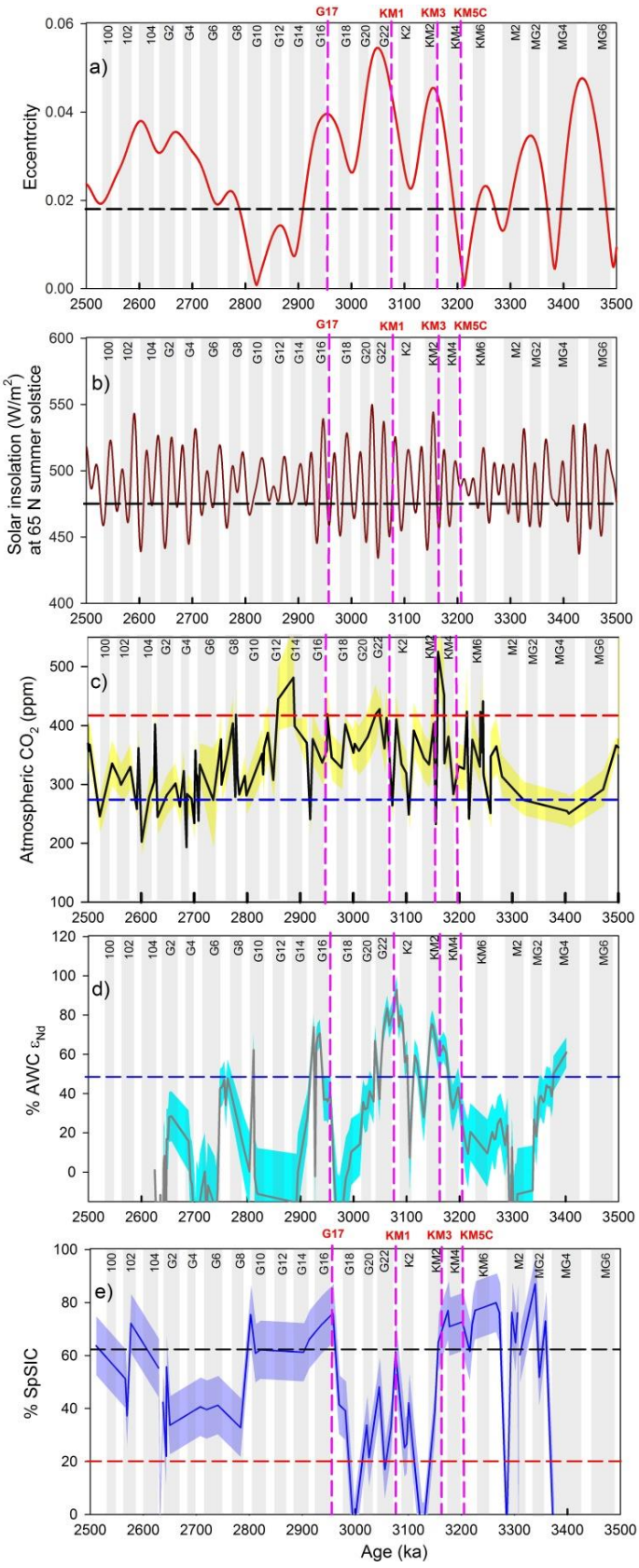
G17
KM1
KM3
KM5C
100
102
104
G2
G4
G6
G8
G10
G12
G14
G16
G18
G20
G22
K2
KM2
KM4
KM6
M2
MG2
MG4
MG6
a)
Eccentrcity
b)
Solar insolation (W/m2) at 65 N summer solstice
c)
Atmospheric CO2 (ppm)
d)
% AWC εNd
e)
% SpSIC
Age (ka)

628

Fig. 5 Role of orbital forcing in modulating watermass exchange and spring sea ice extent. (a) Record of eccentricity (Laskar et al., 2004). Dashed horizontal line represents modern eccentricity. Vertical dashed lines (pink) indicate four interglacial periods KM5C, KM3, KM1 and G17. Among these four interglacial periods, KM5C is most similar to that of the modern orbital forcing(Haywood and Valdes, 2004). (b) Record of solar insolation at 60° N summer solstice (Laskar et al., 2004). Dashed line represents modern value of summer insolation. c) Record of atmospheric pCO_2 derived from boron isotopes ($\delta^{11}B$) (Foster et al., 2017). Yellow band represents error envelops (1σ SD). Black and red colour dashed lines represent pre-industrial CO_2 (280 ppm) and present CO_2 (~410 ppm) level. These forcing parameters are compared with fraction of d) Atlantic Water (%AWC) and (e) Spring sea ice (%).

References

Andersson, P.S., Porcelli, D., Frank, M., Björk, G., Dahlqvist, R., Gustafsson, Ö., 2008. Neodymium isotopes in seawater from the Barents Sea and Fram Strait Arctic–Atlantic gateways. Geochimica et Cosmochimica Acta 72, 2854-2867.

Bachem, P.E., Risebrobakken, B., De Schepper, S., McClymont, E.L., 2017. Highly variable Pliocene sea surface conditions in the Norwegian Sea. Clim. Past 13, 1153-1168.

Bailey, I., Hole, G.M., Foster, G.L., Wilson, P.A., Storey, C.D., Trueman, C.N., Raymo, M.E., 2013. An alternative suggestion for the Pliocene onset of major northern hemisphere glaciation based on the geochemical provenance of North Atlantic Ocean ice-rafted debris. Quaternary Science Reviews 75, 181-194.

Ballantyne, A.P., Axford, Y., Miller, G.H., Otto-Bliesner, B.L., Rosenbloom, N., White, J.W.C., 2013. The amplification of Arctic terrestrial surface temperatures by reduced sea-ice extent during the Pliocene. Palaeogeography, Palaeoclimatology, Palaeoecology 386, 59-67.

Belt, S.T., 2018. Source-specific biomarkers as proxies for Arctic and Antarctic sea ice. Organic Geochemistry 125, 277-298.

Belt, S.T., Brown, T.A., Rodriguez, A.N., Sanz, P.C., Tonkin, A., Ingle, R., 2012. A reproducible method for the extraction, identification and quantification of the Arctic sea ice proxy IP25 from marine sediments. Analytical Methods 4, 705-713.

Belt, S.T., Cabedo-Sanz, P., Smik, L., Navarro-Rodriguez, A., Berben, S.M.P., Knies, J., Husum, K., 2015. Identification of paleo Arctic winter sea ice limits and the marginal ice zone: Optimised biomarker-based reconstructions of late Quaternary Arctic sea ice. Earth and Planetary Science Letters 431, 127-139.

Berends, C.J., de Boer, B., Dolan, A.M., Hill, D.J., van de Wal, R.S.W., 2019. Modelling ice sheet evolution and atmospheric CO2 during the Late Pliocene. Clim. Past 15, 1603-1619.

675 Beszczynska-Moeller, A., Fahrbach, E., Schauer, U., Hansen, E., 2012. Variability in Atlantic
676 water temperature and transport at the entrance to the Arctic Ocean, 1997-2010.
677 Blake-Mizen, K., Hatfield, R.G., Stoner, J.S., Carlson, A.E., Xuan, C., Walczak, M., Lawrence,
678 K.T., Channell, J.E.T., Bailey, I., 2019. Southern Greenland glaciation and Western
679 Boundary Undercurrent evolution recorded on Eirik Drift during the late Pliocene
680 intensification of Northern Hemisphere glaciation. Quaternary Science Reviews 209, 40-
681 51.
682 Cabedo-Sanz, P., Belt, S.T., 2016. Seasonal sea ice variability in eastern Fram Strait over the
683 last 2000 years. arktos 2, 22.
684 Calvo, E., Grimalt, J., Jansen, E., 2002. High resolution U37K sea surface temperature
685 reconstruction in the Norwegian Sea during the Holocene. Quaternary Science Reviews
686 21, 1385-1394.
687 Chen, T.-Y., Frank, M., Haley, B.A., Gutjahr, M., Spielhagen, R.F., 2012. Variations of North
688 Atlantic inflow to the central Arctic Ocean over the last 14 million years inferred from
689 hafnium and neodymium isotopes. Earth and Planetary Science Letters 353-354, 82-92.
690 Clotten, C., Stein, R., Fahl, K., De Schepper, S., 2018. Seasonal sea ice cover during the warm
691 Pliocene: Evidence from the Iceland Sea (ODP Site 907). Earth and Planetary Science
692 Letters 481, 61-72.
693 De Schepper, S., Schreck, M., Beck, K.M., Matthiessen, J., Fahl, K., Mangerud, G., 2015. Early
694 Pliocene onset of modern Nordic Seas circulation related to ocean gateway changes.
695 Nature Communications 6, 8659.
696 Ding, Q., Schweiger, A., L'Heureux, M., Steig, E.J., Battisti, D.S., Johnson, N.C., Blanchard-
697 Wrigglesworth, E., Po-Chedley, S., Zhang, Q., Harnos, K., Bushuk, M., Markle, B., Baxter,
698 I., 2018. Fingerprints of internal drivers of Arctic sea ice loss in observations and model
699 simulations. Nature Geoscience.

700 Dowsett, H., Robinson, M., Haywood, A.M., Salzmann, U., Hill, D., Sohl, L.E., Chandler, M.,
701 Williams, M., Foley, K., Stoll, D.K., 2010. The PRISM3D paleoenvironmental
702 reconstruction. Stratigraphy 7, 123-139.
703 Dowsett, H.J., Cronin, T.M., Poore, R.Z., Thompson, R.S., Whatley, R.C., Wood, A.M., 1992.
704 Micropaleontological Evidence for Increased Meridional Heat Transport in the North
705 Atlantic Ocean During the Pliocene. Science 258, 1133-1135.
706 Dowsett, H.J., Robinson, M.M., Foley, K.M., 2009. Pliocene three-dimensional global ocean
707 temperature reconstruction. Clim. Past 5, 769-783.
708 Dowsett, H.J., Robinson, M.M., Haywood, A.M., Hill, D.J., Dolan, A.M., Stoll, D.K., Chan, W.-L.,
709 Abe-Ouchi, A., Chandler, M.A., Rosenbloom, N.A., Otto-Bliesner, B.L., Bragg, F.J., Lunt,
710 D.J., Foley, K.M., Riesselman, C.R., 2012. Assessing confidence in Pliocene sea surface
711 temperatures to evaluate predictive models. Nature Climate Change 2, 365.
712 Dubois-Dauphin, Q., Colin, C., Bonneau, L., Montagna, P., Wu, Q., Van Rooij, D., Reverdin, G.,
713 Douville, E., Thil, F., Waldner, A., Frank, N., 2017. Fingerprinting Northeast Atlantic water
714 masses using neodymium isotopes. Geochimica et Cosmochimica Acta 210, 267-288.
715 Foster, G.L., Royer, D.L., Lunt, D.J., 2017. Future climate forcing potentially without precedent in
716 the last 420 million years. Nature Communications 8, 14845.
717 François, L., Catherine, J., 2004. Neodymium isotopic composition and rare earth element
718 concentrations in the deep and intermediate Nordic Seas: Constraints on the Iceland
719 Scotland Overflow Water signature. Geochemistry, Geophysics, Geosystems 5.
720 Frank, M., 2002. RADIOGENIC ISOTOPES: TRACERS OF PAST OCEAN CIRCULATION AND
721 EROSIONAL INPUT. Reviews of Geophysics 40, 1-1-1-38.
722 Grøsfjeld, K., De Schepper, S., Fabian, K., Husum, K., Baranwal, S., Andreassen, K., Knies, J.,
723 2014. Dating and palaeoenvironmental reconstruction of the sediments around the
724 Miocene/Pliocene boundary in Yermak Plateau ODP Hole 911A using marine palynology.
725 Palaeogeography, Palaeoclimatology, Palaeoecology 414, 382-402.

726 Haley, B.A., Frank, M., Spielhagen, R.F., Eisenhauer, A., 2007. Influence of brine formation on
727 Arctic Ocean circulation over the past 15 million years. Nature Geoscience 1, 68.
728 Haywood, A.M., Dowsett, H.J., Dolan, A.M., 2016. Integrating geological archives and climate
729 models for the mid-Pliocene warm period. Nature Communications 7, 10646.
730 Haywood, A.M., Hill, D.J., Dolan, A.M., Otto-Bliesner, B.L., Bragg, F., Chan, W.L., Chandler, M.A.,
731 Contoux, C., Dowsett, H.J., Jost, A., Kamae, Y., Lohmann, G., Lunt, D.J., Abe-Ouchi, A.,
732 Pickering, S.J., Ramstein, G., Rosenbloom, N.A., Salzmann, U., Sohl, L., Stepanek, C.,
733 Ueda, H., Yan, Q., Zhang, Z., 2013. Large-scale features of Pliocene climate: results from
734 the Pliocene Model Intercomparison Project. Clim. Past 9, 191-209.
735 Haywood, A.M., Valdes, P.J., 2004. Modelling Pliocene warmth: contribution of atmosphere,
736 oceans and cryosphere. Earth and Planetary Science Letters 218, 363-377.
737 Horikawa, K., Martin, E.E., Basak, C., Onodera, J., Seki, O., Sakamoto, T., Ikehara, M., Sakai,
738 S., Kawamura, K., 2015. Pliocene cooling enhanced by flow of low-salinity Bering Sea
739 water to the Arctic Ocean. Nature Communications 6, 7587.
740 Huber, R., Meggers, H., Baumann, K.H., Henrich, R., 2000. Recent and Pleistocene carbonate
741 dissolution in sediments of the Norwegian–Greenland Sea. Marine Geology 165, 123-136.
742 IPCC, 2013. Climate Change 2013: The Physical Science Basis. Contribution of Working Group
743 I to the Fifth Assessment Report of the Intergovernmental Panel on Climate Change.
744 Cambridge University Press, Cambridge, United Kingdom and New York, NY, USA.
745 Kinnard, C., Zdanowicz, C.M., Fisher, D.A., Isaksson, E., de Vernal, A., Thompson, L.G., 2011.
746 Reconstructed changes in Arctic sea ice over the past 1,450 years. Nature 479, 509.
747 Knies, J., Cabedo-Sanz, P., Belt, S.T., Baranwal, S., Fietz, S., Rosell-Melé, A., 2014a. The
748 emergence of modern sea ice cover in the Arctic Ocean. Nature Communications 5, 5608.
749 Knies, J., Matthiessen, J., Vogt, C., Stein, R., 2002. Evidence of 'Mid-Pliocene (˜3 Ma) global
750 warmth' in the eastern Arctic Ocean and implications for the Svalbard/Barents Sea ice
751 sheet during the late Pliocene and early Pleistocene (˜3 – 1.7 Ma). Boreas 31, 82-93.

752 Knies, J., Mattingsdal, R., Fabian, K., Grøsfjeld, K., Baranwal, S., Husum, K., De Schepper, S.,
753 Vogt, C., Andersen, N., Matthiessen, J., Andreassen, K., Jokat, W., Nam, S.-I., Gaina, C.,
754 2014b. Effect of early Pliocene uplift on late Pliocene cooling in the Arctic–Atlantic
755 gateway. Earth and Planetary Science Letters 387, 132-144.
756 Köseoğlu, D., Belt, S.T., Husum, K., Knies, J., 2018. An assessment of biomarker-based
757 multivariate classification methods versus the PIP25 index for paleo Arctic sea ice
758 reconstruction. Organic Geochemistry 125, 82-94.
759 Lacan, F., Jeandel, C., 2004. Denmark Strait water circulation traced by heterogeneity in
760 neodymium isotopic compositions. Deep Sea Research Part I: Oceanographic Research
761 Papers 51, 71-82.
762 Lambelet, M., van de Flierdt, T., Crocket, K., Rehkämper, M., Kreissig, K., Coles, B., Rijkenberg,
763 M.J.A., Gerringa, L.J.A., de Baar, H.J.W., Steinfeldt, R., 2016. Neodymium isotopic
764 composition and concentration in the western North Atlantic Ocean: Results from the
765 GEOTRACES GA02 section. Geochimica et Cosmochimica Acta 177, 1-29.
766 Lang, D.C., Bailey, I., Wilson, P.A., Chalk, T.B., Foster, G.L., Gutjahr, M., 2016. Incursions of
767 southern-sourced water into the deep North Atlantic during late Pliocene
768 glacial intensification. Nature Geoscience 9, 375.
769 Laskar, J., Robutel, P., Joutel, F., Gastineau, M., Correia, A.C.M., Levrard, B., 2004. A long-term
770 numerical solution for the insolation quantities of the Earth. A&A 428, 261-285.
771 Laukert, G., Frank, M., Bauch, D., Hathorne, E.C., Rabe, B., von Appen, W.-J., Wegner, C.,
772 Zieringer, M., Kassens, H., 2017. Ocean circulation and freshwater pathways in the Arctic
773 Mediterranean based on a combined Nd isotope, REE and oxygen isotope section across
774 Fram Strait. Geochimica et Cosmochimica Acta 202, 285-309.
775 Lawrence, K., Herbert, T., M. Brown, C., Raymo, M., M. Haywood, A., 2009. High amplitude
776 variations in North Atlantic sea surface temperature during the Early Pliocene Warm
777 Period.

778 Lisiecki, L.E., Raymo, M.E., 2005. A Pliocene-Pleistocene stack of 57 globally distributed benthic
779 δ18O records. Paleoceanography 20.
780 Martin, F., 2002. RADIOGENIC ISOTOPES: TRACERS OF PAST OCEAN CIRCULATION AND
781 EROSIONAL INPUT. Reviews of Geophysics 40, 1-1-1-38.
782 Mattingsdal, R., Knies, J., Andreassen, K., Fabian, K., Husum, K., Grøsfjeld, K., De Schepper,
783 S., 2014. A new 6 Myr stratigraphic framework for the Atlantic–Arctic Gateway. Quaternary
784 Science Reviews 92, 170-178.
785 Naafs, B.D.A., Stein, R., Hefter, J., Khélifi, N., De Schepper, S., Haug, G.H., 2010. Late Pliocene
786 changes in the North Atlantic Current. Earth and Planetary Science Letters 298, 434-442.
787 Petrie, R.E., Shaffrey, L.C., Sutton, R.T., 2015. Atmospheric Impact of Arctic Sea Ice Loss in a
788 Coupled Ocean–Atmosphere Simulation. Journal of Climate 28, 9606-9622.
789 Polyakov, I.V., Pnyushkov, A.V., Alkire, M.B., Ashik, I.M., Baumann, T.M., Carmack, E.C.,
790 Goszczko, I., Guthrie, J., Ivanov, V.V., Kanzow, T., Krishfield, R., Kwok, R., Sundfjord, A.,
791 Morison, J., Rember, R., Yulin, A., 2017. Greater role for Atlantic inflows on sea-ice loss
792 in the Eurasian Basin of the Arctic Ocean. Science 356, 285-291.
793 Prescott, C.L., Dolan, A.M., Haywood, A.M., Hunter, S.J., Tindall, J.C., 2018. Regional climate
794 and vegetation response to orbital forcing within the mid-Pliocene Warm Period: A study
795 using HadCM3. Global and Planetary Change 161, 231-243.
796 R Core Team, 2018. R: A language and environment for statistical computing. R Foundation for
797 Statistical Computing. Vienna, Austria URL http://www.R-project.org/.
798 Raymo, M.E., Grant, B., Horowitz, M., Rau, G.H., 1996. Mid-Pliocene warmth: stronger
799 greenhouse and stronger conveyor. Marine Micropaleontology 27, 313-326.
800 Rempfer, J., Stocker, T.F., Joos, F., Dutay, J.-C., Siddall, M., 2011. Modelling Nd-isotopes with a
801 coarse resolution ocean circulation model: Sensitivities to model parameters and
802 source/sink distributions. Geochimica et Cosmochimica Acta 75, 5927-5950.

803 Sato, T., Kameo, K., 1996. Pliocene to Quaternary calcareous nannofossil biostratig- raphy of the
804 Arctic Ocean, with reference to late Pliocene glaciation. W.F. (Eds.), Proc. ODP, Sci.
805 Results 151.
806 Sharma, M., Basu, A.R., Nesterenko, G.V., 1992. Temporal Sr-, Nd- and Pb-isotopic variations in
807 the Siberian flood basalts: Implications for the plume-source characteristics. Earth and
808 Planetary Science Letters 113, 365-381.
809 Smik, L., Cabedo-Sanz, P., Belt, S.T., 2016. Semi-quantitative estimates of paleo Arctic sea ice
810 concentration based on source-specific highly branched isoprenoid alkenes: A further
811 development of the PIP25 index. Organic Geochemistry 92, 63-69.
812 Spielhagen, R.F., Werner, K., Sørensen, S.A., Zamelczyk, K., Kandiano, E., Budeus, G., Husum,
813 K., Marchitto, T.M., Hald, M., 2011. Enhanced Modern Heat Transfer to the Arctic by Warm
814 Atlantic Water. Science 331, 450-453.
815 Tachikawa, K., Jeandel, C., Roy-Barman, M., 1999. A new approach to the Nd residence time in
816 the ocean: the role of atmospheric inputs. Earth and Planetary Science Letters 170, 433-
817 446.
818 Tanaka, T., Togashi, S., Kamioka, H., Amakawa, H., Kagami, H., Hamamoto, T., Yuhara, M.,
819 Orihashi, Y., Yoneda, S., Shimizu, H., Kunimaru, T., Takahashi, K., Yanagi, T., Nakano,
820 T., Fujimaki, H., Shinjo, R., Asahara, Y., Tanimizu, M., Dragusanu, C., 2000. JNdi-1: A
821 neodymium isotopic reference in consistency with LaJolla neodymium.
822 Teschner, C., Frank, M., Haley, B.A., Knies, J., 2016. Plio-Pleistocene evolution of water mass
823 exchange and erosional input at the Atlantic-Arctic gateway. Paleoceanography 31, 582-
824 599.
825 Tütken, T., Eisenhauer, A., Wiegand, B., Hansen, B.T., 2002. Glacial–interglacial cycles in Sr and
826 Nd isotopic composition of Arctic marine sediments triggered by the Svalbard/Barents Sea
827 ice sheet. Marine Geology 182, 351-372.

828 Vogt, C., Knies, J., Spielhagen, R.F., Stein, R., 2001. Detailed mineralogical evidence for two
829 nearly identical glacial/deglacial cycles and Atlantic water advection to the Arctic Ocean
830 during the last 90,000 years. Global and Planetary Change 31, 23-44.
831 Werner, K., Frank, M., Teschner, C., Müller, J., F. Spielhagen, R., 2014. Neoglacial change in
832 deep water exchange and increase of sea-ice transport through eastern Fram Strait:
833 Evidence from radiogenic isotopes.
834 Zhang, Z.S., Nisancioglu, K.H., Chandler, M.A., Haywood, A.M., Otto-Bliesner, B.L., Ramstein,
835 G., Stepanek, C., Abe-Ouchi, A., Chan, W.L., Bragg, F.J., Contoux, C., Dolan, A.M., Hill,
836 D.J., Jost, A., Kamae, Y., Lohmann, G., Lunt, D.J., Rosenbloom, N.A., Sohl, L.E., Ueda,
837 H., 2013. Mid-pliocene Atlantic Meridional Overturning Circulation not unlike modern.
838 Clim. Past 9, 1495-1504.

839

840